

Biocompatibility Assessment and Cellular Uptake of Conjugated Gold-Cockle Shell Derived Calcium Carbonate Nanoparticles for Fluorescent Imaging

Kiranda Hanan Karimah¹, Rozi Mahmud² and Zuki Abu Bakar Zakaria^{1,3}

¹Laboratory of Molecular Biomedicine, Institute of Bioscience, Universiti Putra Malaysia, 43400 UPM, Serdang Malaysia

²Department of Human Anatomy, Institute of Basic Medical College, Chengde Medical University, 067000, Chengde, Hebei, China

³Department of Veterinary Preclinical Sciences, Faculty of Veterinary Medicine, Universiti Putra Malaysia, 43400 UPM, Serdang Malaysia

ABSTRACT

In recent years, fluorescent imaging (FI) has emerged as a major area of interest within the field of medical imaging. FI plays a critical role in molecular imaging. There is evidence suggesting its utility in providing a detailed view of biological and cellular processes at a molecular level. This study aimed to assess the biocompatibility and cellular uptake of conjugated gold-cockle shell derived calcium carbonate nanoparticles (Au-CsCaCO₃NPs) for fluorescent imaging. Researchers have shown a keen interest in the development of targeted multifunctional agents in oncology and near infrared (NIR) fluorescence imaging. This is expected to have significant impact on medical imaging due to the low tissue auto fluorescence and high cellular penetration within the NIR spectrum window. Imaging agents are known to be associated with risks such as non-biodegradability and high toxicity. The synthesized Au-CsCaCO₃NPs were characterized for size and morphology, zeta potential and absorbance in the UV-Vis spectrum. Biocompatibility of Au-CsCaCO₃NPs in cultured human breast carcinoma cells (MCF-7) and mouse embryonic fibroblast cells (NIH-3T3) was evaluated using lactate dehydrogenase (LDH) and reactive oxygen species (ROS) bioassays for toxicity analysis. Cellular morphology and uptake was examined by fluorescence and confocal microscopy. Cells were able to take up nanoparticles within their cellular compartments. Further, increased cell death was observed in Au-CsCaCO₃NPs-treated MCF-7 cells relative to Au-CsCaCO₃NPs-treated NIH-3T3 cells. The Au-CsCaCO₃NPs were biocompatible, environmentally friendly and easily synthesized. These results suggest Au-CsCaCO₃NPs may have significant cellular imaging utility

Keywords: Au-CsCaCO₃NPs; Nanoparticle biocompatibility; LDH; ROS; Cellular uptake; Fluorescent imaging

*Correspondence to: Zuki Abu Bakar Zakaria, Laboratory of Molecular Biomedicine, Institute of Bioscience, Universiti Putra Malaysia, 43400 UPM, Serdang Malaysia; E-mail: zuki@upm.edu.my

Received: Sep 28, 2020; **Accepted:** Oct 26, 2020; **Published:** Oct 31, 2020

Citation: Karimah KH, Mahmud R, Zakaria ZAB (2020) Biocompatibility Assessment and Cellular Uptake of Conjugated Gold-Cockle Shell Derived Calcium Carbonate Nanoparticles for Fluorescent Imaging. *J. Nanomed. Nanotech. Nanomat.* 1(1): 105.

Copyright: ©2020 Karimah KH, et al. This is an open-access article distributed under the terms of the Creative Commons Attribution License, which permits unrestricted use, distribution, and reproduction in any medium, provided the original author and source are credited.

INTRODUCTION

In recent years, nanoparticles ranging in size from 10-100 nm, [1] have shown great promise in biomedical imaging, regenerative medicine, scaffold studies, drug delivery, therapeutics, and tissue engineering [2-9]. In particular, the last decade has seen a growing trend towards using nanoparticles for imaging [10, 11], with considerable literature focused on biogenic nanoparticles such as aragonite calcium carbonate nanoparticles [12] and gold nanoparticles (AuNPs) [13]. Aragonite is one of the polymorphs of calcium carbonate that naturally and richly exists (95 - 98 %) in cockle shell (*Anadara granosa*), a mollusc found in Malaysia [14]. The effects of using calcium carbonate nanoparticles for imaging has been described with the Eu^{3+} -doped calcium carbonate cubic nanoparticles produced by carbonation synthetic route, and the photoluminescence properties characterised by scanning electron microscope and x-ray diffractometer [15-17]. In other related studies, it was demonstrated in the technique used for the development of fabricated oxygen sensitive polymer nano capsules by means of layer by layer (LBL) tactic using vaterite calcium carbonate nanoparticles as templates. Additionally, arguing that the buffer used played a decisive role in maintaining their integrity and that the nanoparticles were utmost stable in alkaline sodium hydrogen carbonate [18]. A more current study by Savelyeva and co-workers for biomedical use involved the formation of porous vaterite calcium carbonate coverings on whole surface and interior of electrospun poly (ϵ -caprolactone) (PCL) fiber surfaces by using

ultrasound [19]. The method described that the difference in experimental settings such as reagent concentration, treatment and time, allow for control of the calcium carbonate of vaterite or calcite polymorph and has proven successful on PCL - CaCO_3 (calcium carbonate) scaffolds [20-22]. Similarly, a recent comprehensive study of chitosan calcium carbonate nanoparticles modified with diacid, centered on L-phenyl aniline (2 - 8 wt %) using different mass ratios formed by ultrasound agitation [23]. In addition, also found that the nanoparticles revealed thermal stability and a notable adsorption capacity due to presence of active spots like the amino and carbonyl groups [24-26]. In regards to the AuNPs, there is a relatively small body of literature that is concerned with the development of AuNPs bioconjugates and their potential use in imaging or other biomedical applications [27, 28]. Also, due to their low or non-significant toxicity are increasingly being used in diagnosis, therapeutics, disease treatment, and targeted drug delivery systems [28-33]. In addition, AuNPs bioconjugates maintain high stability upon interaction with biomolecules such as proteins and antibodies [34,35]. Major attention being on the AuNPs surface plasmon resonance property, which pays particular focus to designing diagnostic biomaterials, drug targeting agents, therapeutics, and contrast agents [36-42]. Furthermore, existing works on AuNPs and their conjugates has extensively been employed in agriculture to enhance visual detection of pesticides, food industry to detect contaminants, and extension of

food shelf life [43, 44]. However, recent developments in biomedical imaging reason that there is existence of limitations concerned with the current imaging probes meant for clinical usage. These include non-biodegradability or slow excretion and high toxicity challenging the production of a strong imaging signal compromising their further evolution into clinical use [10]. In addition, research investigations suggest that there are also a number challenges associated with targeted tumor nanoparticles administered by intravenous route due to interaction with an intricate atmosphere [45].

These include clearance of targeted nanoparticles by the phagocytes; either by effectively removing nanoparticles from circulation leaving a trivial portion at the tumor sites or by long retention of the nanoparticles potentially developing into complications like toxicity [46]. Secondly, tumor physiological properties like antigen expression and tumor permeability that stop the buildup of the nanoparticles or drug delivery in the region [47-49]. It has also been elaborated in a prior study that nanoparticles in blood circulation, habitually bind to plasma proteins (opsonization) that are phagocytosed within the blood, spleen, bone marrow and liver [50]. Similar studies have shown techniques that alleviate these limitations, by embracing the stabilization of particle dispersions using coatings, understanding the outcome of the nanoparticles in the blood stream and their physiochemical properties thus, a substantial need to produce biocompatible nanoparticles with ideal features [51-54]. Herewith, gold near infrared conjugated cockle shell-derived calcium carbonate

nanoparticles (Au-CsCaCO₃NPs) are prepared and assessed for *in vitro* biocompatibility using assays such as lactate dehydrogenase and reactive oxygen species. Cellular uptake of the Au-CsCaCO₃NPs, evaluated using fluorescent and confocal imaging. Primarily, the Au-CsCaCO₃NPs development is prompted by the need for cost efficient and biocompatible nanomaterial for imaging. The preparation utilizes method friendly approaches such as, the classic Turkevich method [55] and dodecyl dimethyl betaine (BS - 12). The Au-CsCaCO₃NPs potential use for fluorescent imaging is also elaborately discussed.

MATERIALS AND METHODS

Materials and chemicals

The gold colloid solution was purchased from prima nexus Sdn Bhd (Malaysia). Indocyanine green dye (ICG) was purchased from Sigma-Aldrich (Steinheim, Germany). DAPI (4', 6-diamidino-2-phenylindole), Prolong gold antifade reagent, acridine orange (AO) and propidium iodide (PI) from Sigma-Aldrich (USA). Dulbecco's modified Eagle's medium (DMEM), trypsin, fetal bovine serum (FBS), antibiotics combination (glutamine 100 mmol/L, penicillin 100 U/mL and streptomycin 100 µg/mL), and phosphate-buffered saline (PBS) were purchased from Naclai Tesque, Inc., Kyoto, Japan. Lactate Dehydrogenase (LDH) Assay and Reactive Oxygen Species (ROS) Assay were purchased from Cell Biolabs, Inc., San Diego CA, USA. Breast cancer cell line (JCRB: MCF-7) and the fibroblast cell line (JCRB: NIH-3T3) were commercially purchased from the Japanese Collection Research Bioresource

(JCRB). All chemicals used were of analytical grade unless mentioned otherwise in the experiments.

Incorporation of NIR dye and Synthesis of Conjugated Gold-Cockle Shell-Derived Calcium Carbonate Nanoparticles (Au-CsCaCO₃NPs)

The synthesis of cockle shell derived calcium carbonate nanoparticles was performed as described by Islam and colleagues (2013) [56]. Gold nanoparticle synthesis was performed using the method described by Verma and colleagues (2014) [57]. Approximately 0.2 g cockle shell derived calcium carbonate nanoparticles was mixed in 20 ml gold nanoparticle solution, by the method of Cai and colleagues (2006) [58]. Approximately 5 mg indocyanine green (ICG) was added to the mixture. The solution was sonicated for 20 minutes and incubated for 3 days on magnetic stirrer at 200 rpm. The mixture was further ultra-centrifuged for 10 minutes at 10,000 rpm resulting in a light-green-purplish, (Au-CsCaCO₃NP) nano-composite. The supernatant was decanted and pellet washed multiple times with deionised water. The prepared nano-composite was dried in the oven for 4 days and stored in oven for later use.

Characterisation of Au-CsCaCO₃NPs

Transmission Electron Microscope (TEM): The nanoparticle size and morphology was analysed using transmission electron microscope (TEM). The nano conjugate was dispersed in absolute alcohol and sonicated for 40 minutes. About 5 µl of the suspended sample solution was pipetted out on to copper grid

specimen mount. The sample was viewed under TEM (Hitachi H-7100).

Zeta Potential and Measurement Size Distribution:

The analysis for the synthesized nano conjugate was done using zetasizer Nano ZS (Malvern Panalytical). The nano conjugate was suspended in deionised water and sonicated for 1 hour. The homogenous suspension was then deposited into the zeta cuvette and examined for zeta potential and size distribution by intensity.

UV-VIS Spectrophotometer: The presence of different analytes of the nano conjugate were monitored using UV-Vis spectrophotometer (UV-2600) at wavelengths ranging from 300 - 800 nm.

***In vitro* Cell Culture and Biocompatibility Studies:**

Human breast carcinoma cells (JCRB: MCF-7) and normal mouse embryonic fibroblast cells (JCRB: NIH-3T3) from receipt (P0) were cultured to post-receipt passage 5 (P5) in DMEM (high glucose) supplemented with 10% FBS and antibiotics combination. The cultured flasks (Eppendorf culture T-25 and T-75) were then placed in an incubator with 5% carbon dioxide at 37°C (Thermo Fisher Scientific LPG, Hudson, New Hampshire, USA) until the flasks reached 80% - 90% cell confluence, at which time, the cultured cells were further used for seeding and treatment.

2.4.1 Cells Seeding and Treatment: Cultured cells were detached using trypsin and seeded into 96-well plates at a density of 1×10^5 cells per well. The 96-well plates were then placed into the 5% carbon dioxide incubator at 37°C for 24 hours. The medium was removed and the cells were treated and co-cultured in

replicates with Au-C₆₀CaCO₃NPs suspension (concentration of 1 mg/ml in 10% serum free DMEM media) for a period of 24 hours, 48 hours, and 72 hours. After exposure, the medium in the wells was aspirated and monolayers were washed with PBS. Medium was replaced for cell use in the LDH assay and ROS assay.

Lactate Dehydrogenase Assay (LDH): Published LDH studies were identified using a search strategy developed by Allen and colleagues (1994) [59]. MCF-7 cells and NIH-3T3 cells in 96-well plates were incubated for 72 hours after treatment with 0, 50, or 100 µg nanoparticle solutions. The 96-well plates were cleared of all previous media and cell membrane integrity assessed using the protocol adapted by Smith and colleagues (2011) [60]. The protocol measures the amount of LDH released by the lysed cells as a measurement of cell damage.

Lactate Dehydrogenase Treatment Protocol: The 96 - well plates were removed from the incubator with previous treatment. Sterile water and Triton X-100 provided were added to each well in triplicate for the pre-seeded and treated plates as shown in table 1 below.

Reagent	Experimental Sample	Negative Control	Positive Control
Sterile Water	15 µl	15 µl	nil
Triton X-100	nil	nil	15 µl

Table 1: Lactate Dehydrogenase Treatment Protocol.

The plates were incubated for 10 minutes at room temperature. Approximately, 90 µl of media was carefully transferred from each well to clean 96-well plates suitable for microplate reader. Around 10 µl of

LDH assay reagent was added to the wells and allowed to incubate for 1 hour. After incubation, the plates were placed on a shaker for 10 minutes and optical density of the solution was measured with a microplate reader at 450 nm. The values were recorded and a graph plotted with Excel.

Reactive Oxygen Species Assay (ROS)

Reactive Oxygen Species Treatment Protocol

Preparation of Reagents: 1X DCF-DA (20X DCF-DA stock solution diluted to 1x in serum free DMEM media and mixed uniformly using sonicator vortex). Hydrogen peroxide (H₂O₂) dilutions were prepared in serum-free DMEM.

Preparation of Standard Curve: Ten-fold serial dilutions of DCF standards were prepared in a concentration range to 10 µM by diluting the 1 mM DCF stock in serum-free DMEM shown in Table 2. A 0 µM control was also prepared without DCF.

Standard Tubes (T)	DCF Standards (µl)	DMEM Serum Free Media (µl)	DCF (nM)
1	10	990	10000
2	100 of T1	900	1000
3	100 of T2	900	100
4	100 of T3	900	10
5	100 of T4	900	1
6	100 of T5	900	0.1
7	100 of T6	900	0.01
8	0	1000	0

Table 2: Preparation of Standard Curve.

Preparation of DCF Standards: 75 µl of each DCF standard was transferred to a 96-well plate followed by

75 μ l of the 2X cell lysis buffer. Fluorescence was measured at 480 nm excitation and 530 nm emissions.

Assay Protocol

DCF Dye loading: The 96-well plates were cleared of all previous media and washed twice with PBS. 100 μ l of 1X DCF-DA prepared solution was added to the cells and incubated for 45 - 60 minutes at 37°C. The 96-well plates were cleared of all solutions and washed twice with PBS. The DCF-DA loaded cells were treated with the prepared hydrogen peroxide in 100 μ l media.

Quantitation of Fluorescence: After treatment with the oxidant, media was removed from the 96-well plates and plated were washed twice well with PBS. 100 μ l of media and 100 μ l of 2X cell lysis buffer was added to each well, mixed thoroughly, then incubated for 10 minutes. 150 μ l of the mixture was then transferred into a clean 96-well plate for fluorescent measurement. The fluorescence was recorded at 480 nm excitation and 530 nm emission. The experiment was conducted in triplicate.

***In vitro* Confocal Imaging and Cellular Uptake of the Gold Near Infrared Conjugated Cockle Shell-derived Calcium Carbonate Nanoparticles (Au-CsCaCO₃NPs)**

Breast cancer cells, MCF-7, were seeded into 6-well plates in DMEM. Upon reaching 80% cell confluence, the medium was removed then replaced with 1ml of fresh culture medium supplemented with 25 mM HEPES containing Au-CsCaCO₃NPs suspension and incubated at 37°C for 6 hours. The cells were washed in PBS three times before analysis by fluorescent and confocal microscopy. Fluorescent emission was visualized using a

fluorescent microscope and images were recorded for quantification of conjugate nanomaterial uptake by the cells (Immunofluorescence Microscopy System, Tokyo, Japan).

Fluorescent Preparation Protocol: The cells were seeded onto 4-well chambered sterile slide (SPL life sci, made in Korea) and incubated for 24 hours overnight. The medium was removed and the cells were treated in replicates with Au-CsCaCO₃NPs suspension for a period of 72 hours. After exposure, the medium in the wells were aspirated and washed with PBS twice. The cells were re-suspended after trypsinization and 0.5 ml of Devil's stain [1:1 ratio of AO and PI] was added to each well for 60 minutes at room temperature. Afterwards, a drop was taken and mounted on clean slide with coverslip. The slides were examined using fluorescence microscopy (Immunofluorescence microscopy system, Tokyo, Japan).

Confocal Preparation Protocol: The cells were seeded onto 4-well chambered sterile slides (SPL life sci, made in Korea) and incubated for 24 hours. The medium in the wells was removed and the cells were treated in replicates with Au-CsCaCO₃NPs for a period of 72 hours. After exposure, the medium in the wells was aspirated and washed with PBS twice. The cells were fixed in 3.7% pre-cooled paraformaldehyde at room temperature for 15 minutes then washed twice with PBS. 500 μ l of Devil's stain was added to each well for 60 minutes at room temperature. Each well was washed twice with PBS followed by a counter stain of 50 μ l prepared intermediate DAPI (4',6-diamidino-2-phenylindole) for 2 minutes at room temperature. The

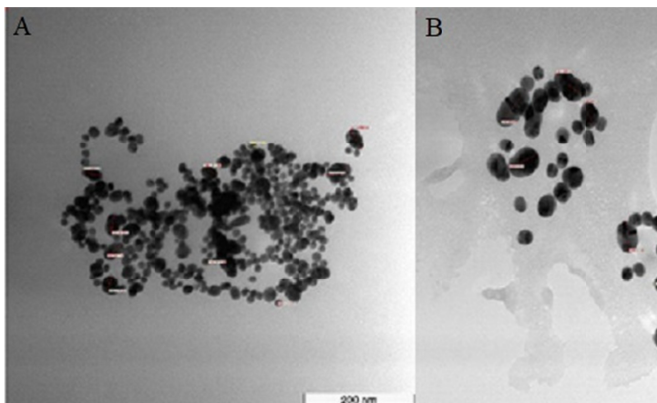
wells were washed three times with PBS in dark and coverslips were mounted with Prolong gold antifade reagent (Molecular probe, USA). The slides were examined using a confocal laser-scanning microscope (Zeiss, Germany).

Statistical Analysis: All data analysis was performed using SPSS software (Version 10, Chicago, USA) using *t*-test, one-way ANOVA, and regression analysis. Experiments were done in triplicate. Data is expressed as mean \pm standard deviation ($M \pm SD$). The level of statistical significance was $p < 0.05$, unless mentioned otherwise.

RESULTS AND DISCUSSION

Transmission Electron Microscope (TEM)

The TEM micrographs in figure 1 show the shape and size of the synthesized gold conjugated-cockle shell-derived calcium carbonate nanoparticles (Au-CsCaCO₃NPs) prepared with 100% acetone. The Au-CsCaCO₃NPs are well dispersed with an average



Figures 1A and 1B: TEM micrographs of the conjugated Au-CsCaCO₃NPs synthesized via citrate reduction, chemical precipitation and mechanical methods, which show well-dispersed Au-CsCaCO₃NPs with an average diameter size of 32 ± 13 nm.

diameter of 32 ± 13 nm with the variation in size attributed to the synthesis conditions.

These results suggest that there is an association between the nanoparticles leading to conjugation and confirm that our synthesized Au-CsCaCO₃NPs are of nanoparticle size. The most obvious finding to emerge is that the conjugated nanoparticles showed absorbed gold nanoparticles inside calcium carbonate nano-sphere matrix with excellent particle size, good homogeneity and surprisingly, not much differences in particle size. A possible explanation for the uniquely obtained homogenized nano-size could be the controlled synthesis conditions and the mechanical approach employed resulting in an average and continuous shear force within the particles, which accelerated their uniform breakdown and their dispersity. The mechanical method has been noted as an excellent alternative for synthesizing more pure and uniform nanoparticles with lesser impurities to the chemical synthesis [61]. The nanoparticle dispersion could also be due to the negatively charged layer of citrate ions aiding in the repulsion of nanoparticles from each other, as suggested by Eaqub-Ali and colleagues (2014) [62]. Nanoparticle physical and chemical properties greatly rely upon the conditions and method of synthesis [63]. Recent studies have documented particle dispersion to be due to electrostatic repulsion and the conjugate hydration surface layer, preventing aggregation and increasing conjugate stability [64]. Rawat and colleagues (2016) [65] found that the citrate capping reagents affected in the synthesis, which allowed for more dispersity and stability of the conjugated nanoparticles. Furthermore,

the citrate reduction method has been notably known for preparing different sized, citrate-capped, spherical shaped, and homogeneously dispersed nanoparticles [57]. These results are in agreement with Cai and colleagues (2006) [58] who showed exceptional gold nanoparticle size absorbed inside the matrix of calcium carbonate microspheres.

Zeta Potential and Measurement of Size Distribution

The stability and assessment of the Au-CsCaCO₃NPs surface charge and size distribution by intensity is shown in figure 2 and Table 3. The surface charge was -16.5 mV, and the poly dispersity index (PDI) was < 0.5.

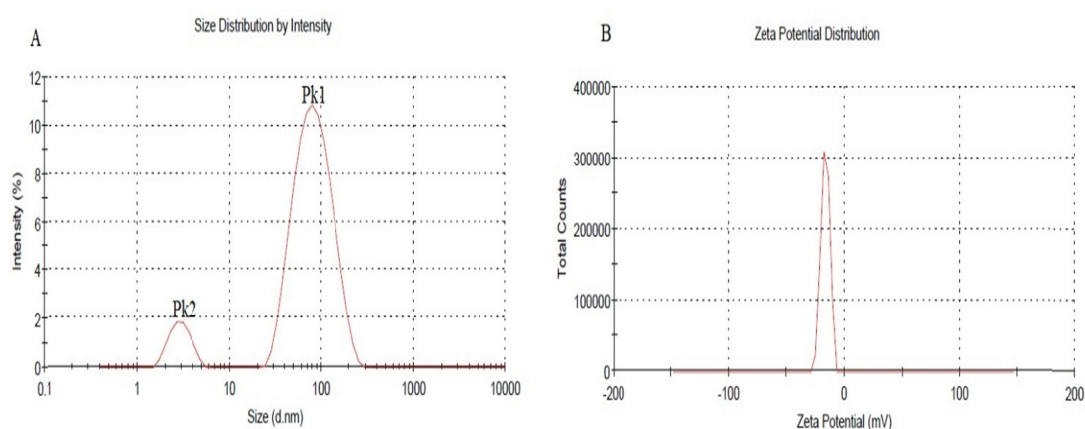


Figure 2: Size distribution by intensity showing two peaks (A) and zeta potential indicating surface charge (B) of the Au-CsCaCO₃NPs.

This analysis set out with the aim of evaluating the importance of zeta potential in assessing the surface charge and stability of the synthesized nanoparticles where previous studies observed inconsistent results of the nanoparticles. The stability of the conjugated nanoparticles could be established by zeta-potential measurements along with UV-Vis spectrophotometer [66]. A prior study has shown that the intensity of the light scattered is relative to the six power of their particle size, and also the larger particles give a greater signal than smaller particles [67]. Interestingly, the current findings also found that highly positive and

highly negative zeta potential indicates a decrease in aggregation, and increased stability.

showed that the nanoparticles have a high negative surface charge which further displayed nanoparticle stability. This may be explained by the fact that the presence of more electro-repulsion between the particles ultimately displayed lesser agglomeration. This outcome reflects that of Hoque and colleagues (2013) [68] who very stable [69, 70]. The results in Table 3 also show that the size of the nano conjugate in water as measured by the dynamic light scattering (DSL) and the zeta potential which corresponds to the negatively charged nanoparticles.

Zeta Potential		Zeta Size Distribution			
Surface Charge (mV) \pm SD	Area (%)	Peak (Pk)	Size (d. nm)	% Intensity	Width (d. nm)
-16.5 \pm 3.66	100	1	89.99	90.9	40.62
		2	3.983	9.10	0.758
		3	0.000	0.00	0.000
		PDI	0.491		

Table 3: Surface Charge and Size Distribution by light Intensity of the Au-CsCaCO₃NPs.

A high negative zeta potential relates to the repulsive interaction between the nanoparticles focused on preventing agglomeration of the nanoparticles, thus exhibiting stability during the incubation period in water [71, 72]. The high negative surface charge of the nanoparticle suspensions not only indicates high stability, but also suggests less toxicity to normal cells [73]. However, another possible explanation for these results could be the dispersity of the nano conjugate material in solution due to electric repulsion that electrically stabilizes the nanoparticles and physiochemical differences of the nanoparticles could be attributed to the synthesis methods used. Similarly, Zhang and colleagues (2008) [74] who exposed the understanding of the overall stability, nanoparticle shelf life, particle interactions between the charged particles and their implications. This outcome is contrary to that of Das and colleagues (2011) [75] who showed larger nanoparticle size >100 nm with extremely high positive charge suggesting to prevent aggregation which does not appear to be our case. Also, in agreement with findings reported by Isa and colleagues (2016), [76] which emphasize that higher negative or positive values of zeta-potential indicate stability and averts aggregation of particles, because of electric repulsion that electrically

stabilizes the nanoparticles dispersion. It can, therefore, be positively assumed that the conjugated nanoparticles have good stability.

Uv-Vis Spectrophotometer

The Uv-Vis spectrophotometer spectra of gold nanoparticles (AuNPs) and Au-CsCaCO₃NPs were compared in order to distinguish the different absorption-wavelength crests of the nanoparticles. The AuNPs spectrum illustrates a sharper average absorption peak at 522 nm whereas the Au-CsCaCO₃NPs spectrum shows a wider utmost absorption peak between 525 - 536 nm as revealed in figure 3.

Altogether, this outcome suggests that there is an

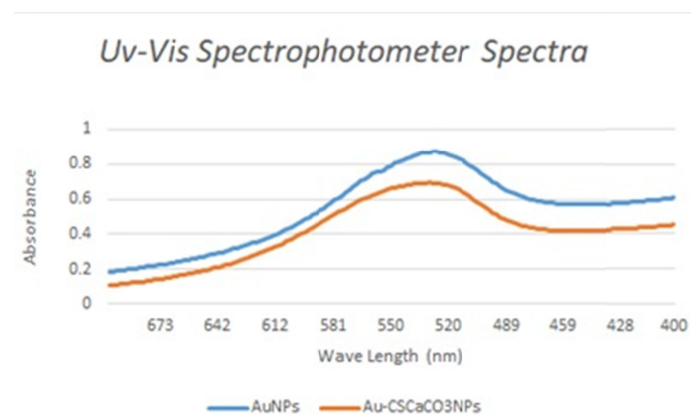


Figure 3: Uv-Vis spectra of AuNPs and Au-CsCaCO₃NPs shows absorption peaks at 522 nm and between 525 - 536 nm respectively for the nanoparticles.

association between the AuNPs and Au-CsCaCO₃NPs indicating the presence of the desired synthesized nanoparticles.

A shift in the maximal absorbance wavelength of the conjugated nanoparticles in comparison to naked AuNPs was observed as indication of aggregation [66]. In accordance with the present results, previous studies have validated that gold nanostructures have a wide light absorbance range but gold plasmon resonance absorbance is significantly observed from 500 - 520 nm wavelength [57, 77] and what is surprising is that our conjugated Au-CsCaCO₃NPs displayed absorption peak between 525 - 536 nm wavelength. A possible accountability for these results could be explained by the formation of the conjugated nanoparticles as the AuNPs enter the matrix of the cockle shell- derived calcium carbonate nanoparticles (CsCaCO₃NPs). Whose diameter is influenced by the varying nanoparticle concentrations suggesting increased AuNPs concentration, more absorption into the CsCaCO₃NPs and as a result leading to increased absorption. Additionally, in the near infrared visible spectral region, at which light is easily attenuated by the tissue and it has been significantly reported that absorption peaks could shift as described by Smith and colleagues (2010) [78]. However, in contrast to earlier findings, no clear evidence of near infrared (NIR) was detected in the conjugated nanoparticles. Possibly, the absorption spectrum of nanoparticles could shift depending on color, morphology, and size with the utilization of the plasmon resonance property. Furthermore, the nanostructures with NIR photo-thermal properties have

been identified to be capable of scattering light strongly, which has significant applications in biomedical imaging [79].

Cell Culture

Lactate Dehydrogenase Assay (LDH)

This analysis was intended to evaluate the cell membrane integrity of human breast carcinoma cell line (MCF-7) and mouse embryonic fibroblast cell line (NIH-3T3) treated with the synthesized Au-CsCaCO₃NPs by analyzing the lactate dehydrogenase (LDH) levels after exposure to the 0, 50, or 100 µg for 72 hours (figure 4).

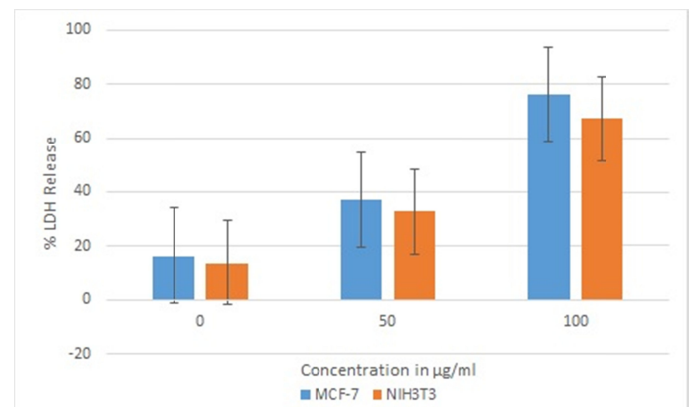


Figure 4: Comparative LDH released by Au-CsCaCO₃NPs treated MCF-7 cells and Au-CsCaCO₃NPs treated NIH3T3 cells, showing higher LDH % release with MCF-7 as compared to NIH3T3. The level of statistical significance was $p < 0.05$.

The results suggest that the LDH percentage (%) release of MCF-7 cells treated with Au-CsCaCO₃NPs was slightly higher than that of the Au-CsCaCO₃NPs treated NIH3T3 cells.

The results show biocompatibility assessment of the nanoparticles on the cell lines by evaluating the cell membrane integrity. It was initially established that a normal cell membrane is impermeable to lactate

dehydrogenase (LDH) release activity, also a common and standard biocompatibility test used *in vitro* cytotoxicity studies [59]. A bioassay used to quantify the number of dead cells through LDH leaked from the damaged cell plasma membrane correlating to cell death rate [80]. This study, surprisingly illustrates that the conjugated nanoparticles LDH % release of NIH3T3 was significantly lower compared to that of MCF-7. This result could be clarified by the fact that nanoparticle internalization, could prompt intracellular responses along with the growing accumulation of LDH within the cytosol facilitating the reverse conversion of lactate to pyruvate following reduction of NAD^+ to NADH within the cell. Furthermore, these results offer a promising possibility of conjugated particles for biomolecular and cellular biomedical applications such as imaging and drug delivery. Several reports have proven LDH to oxidize lactate to pyruvate while consuming NADH [81]. The cytosolic enzymes are released into the extracellular fluids only when the cell membrane integrity is lost, assessing the cell membrane integrity by measuring the amount of LDH released from the lysed cells which are directly proportional to the damaged cells [60]. Recent literature on LDH findings with work done on cancer cell line HeLa and MCF-7 using nanoparticle delivery systems and surface functionalized nanoparticles have reported higher LDH leakages [82]. In the same regard, high LDH leakages have been confirmed with MCF-7 as a result of metallic nanoparticles [83] but also known reports have argued, lower LDH release with slight compromise of the cell membrane integrity by fibroblast cells L929 [84].

However, this outcome is contrary to that of Lanari and colleagues (2001) and Smith and colleagues (2001) [85-87] who found that LDH assay studies on HeLa, MCF-7, and NIH3T3 using gold nano-ribbons revealed utmost LDH release in HeLa than MCF-7 and furthermore, reporting no significant difference with the LDH% release between MCF-7 and NIH3T3 [88]. In addition, previous studies on nano material have been reported to induce high LDH levels which has been attributed to nanoparticle morphology inducing oxidative stress [89]. Therefore, the current LDH results revealed no toxicity as demonstrated with the conjugated nanoparticles.

Reactive Oxygen Species (ROS)

The objective of ROS experimental assay analysis was to further investigate the reactive oxygen species of Au-C_sCaCO₃NPs on MCF-7 and NIH-3T3 through measuring the relative fluorescence units (RFU) adapted from the standard as presented in figure 5 below.

The results demonstrate that Au-C_sCaCO₃NPs treated MCF-7 cells exhibited higher ROS release relative to the Au-C_sCaCO₃NPs treated NIH-3T3 cells (figure 6). They displayed minimal ROS release, less than 400 RFU at concentration of 100 μg , relative to MCF-7.

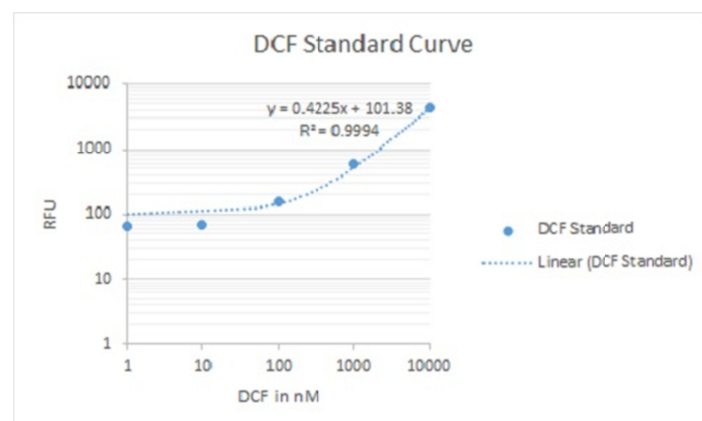


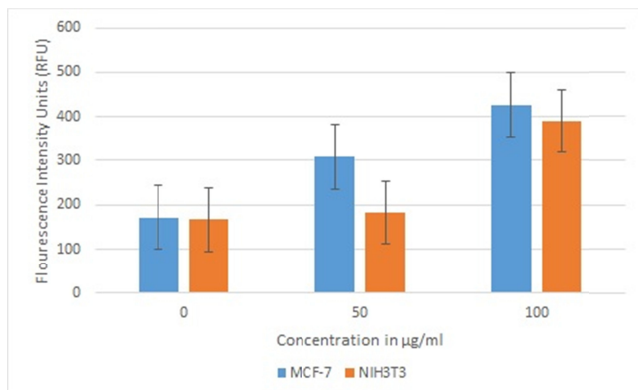
Figure 5: DCF Standard curve.

Figure 6: Comparative ROS generation by Au-CsCaCO₃NPs treated MCF-7 cells and Au-CsCaCO₃NPs treated NIH3T3 cells, showing higher ROS generation with MCF-7 as compared to NIH3T3. The level of statistical significance was $p < 0.05$.

Collectively, the overall reactive oxygen species assay findings of the nanoparticles on MCF-7 and NIH-3T3 provide useful understanding into oxygen metabolism. Reactive oxygen species refer to chemicals, radicals, or molecules that comprise reactive oxygen compounds such as peroxides resulting from normal oxygen metabolism with vital roles in homeostasis and cell signaling [90]. ROS generation by the NIH-3T3 was significantly lower than MCF-7 and showed consistent ROS generation also in agreement with previous biocompatibility results further highlighting the remarkability of Au-CsCaCO₃NPs. These results could be explained by the fact that the internalization of the nanoparticles possibly induced oxidative stress which in turn triggered cell death displayed in the results. This study supports evidence that induction of environmental stress drastically increases ROS levels causing substantial cellular damage also known as oxidative stress [91] and also corroborates the findings of previous works in which cancer cells generate high levels of

ROS. This is further explained by increased metabolic activities of oxidases and peroxisomes, mitochondria malfunctioning or cellular dysfunction [92-94]. Consistent with prior literature, this research also found works that reported nanoparticle cellular uptake to induce mitochondrial membrane permeability and disrupting the respiratory chain causing apoptosis [95]. Similarly, it has been argued for local cancer therapy that Burkitt lymphoma B cells and epithelial breast cancer cells caused possible damage using targeted irradiation and gold nanoparticles causing high ROS generation leading to cellular necrosis or apoptosis but while sustaining minimal damage to adjacent, particle-free tissue [96]. Additionally, it has been established that carbon and metallic nano material generate minimal ROS. However, their morphology, size, positive surface charges, aggregation, cellular interaction and nano-metallic ions influence oxidative stress release causing physiological dysfunction of the cell which in turn prompts DNA damage [97, 98]. This finding is contrary to previous studies which have suggested that there is significantly higher generation of ROS over time by metallic nanomaterial as described by Xue and colleagues (2016) [99] with works on human liver HepG2 cells. In the same regard no significant effects were found with works on NIH3T3 cells [100]. Conclusively, these results offer competencies of the conjugated nanoparticles for cellular imaging applications.

Fluorescent Imaging and Confocal Imaging

The purpose of fluorescent and confocal imaging of MCF-7 and NIH3T3 was to morphologically visualize

cell death and the possibility of cellular uptake of the nanoparticles using AO and PI double staining method and DAPI. The results in the MCF-7 fluorescent micrographs display most live cells with the control unlike with the Au-C_sCaCO₃NPs treated cells which show more cell death as revealed in figure 7.

The NIH3T3 fluorescent micrographs show more live cells with the control and Au-C_sCaCO₃NPs as revealed in figure 8. However, the most interesting fact is that, the

MCF-7 treated cells observed more cell deaths in comparison to the NIH3T3 treated cells counterparts. The findings in the confocal micrographs are an overview of the mechanisms of intracellular uptake by MCF-7 and NIH3T3 which show appearance of the nanoparticles inside the cellular compartment under four different fluorescent filters (blue, green, red and merged filter) unlike the controls as indicated by arrows within their figures illustrated in figures 9 - 12.

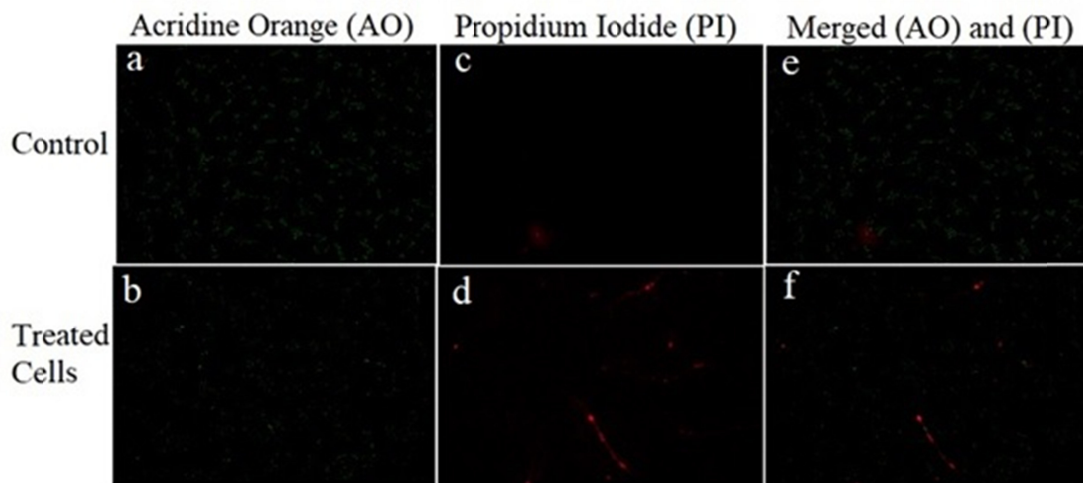


Figure 7: Fluorescent images of MCF-7 cells after treatment with Acridine Orange (AO), Propidium Iodide (PI) and merged (PI and AO). Images (a) and (b) show live cells after after treatment with AO, control having more cells as as compared to Au-C_sCaCO₃NPs treated cells. Images (c) and (d) show dead cells after after treatment with PI, control having less cells as compared to Au-C_sCaCO₃NPs treated cells. Images (e) and (f) show both live and dead cells after merging. Magnification $\times 10$, scale bar 100 μm .

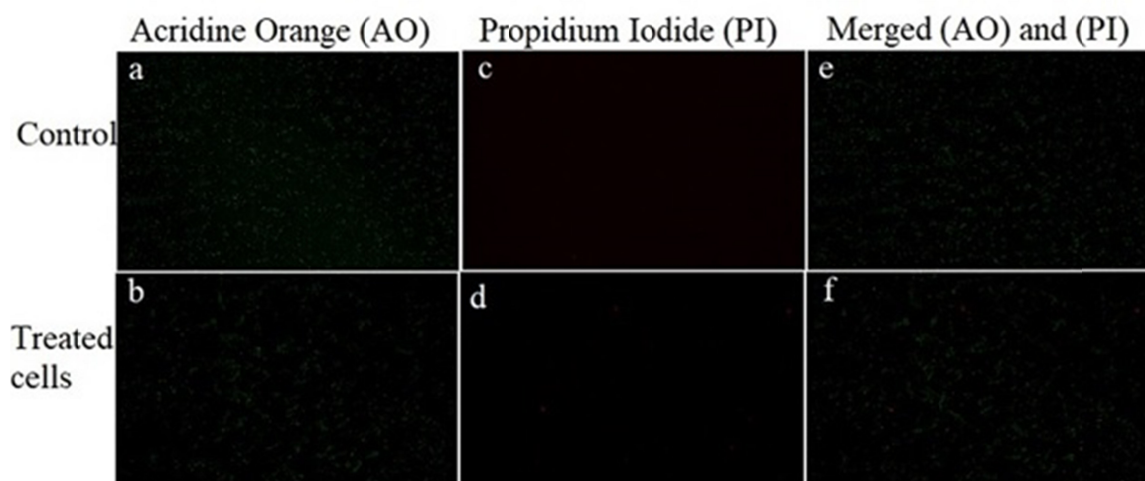


Figure 8: Fluorescent images of NIH3T3 cells after treatment with Acridine Orange (AO), Propidium Iodide (PI) and merged (PI and AO). Images (a) and (b) show live cells after treatment with AO, Au-CsCaCO₃NPs treated cells showing no much difference with the control. Images (c) and (d) show less or no dead cells after treatment with PI. Images (e) and (f) show both live and dead cells after merging. Magnification $\times 10$, scale bar 100 μm .

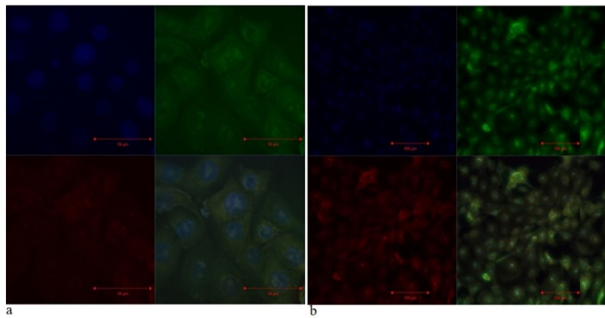


Figure 9: Confocal micrographs of MCF-7 control showing cellular morphology under different fluorescent filters using DAPI (blue), AO (green), PI (red) and merged filter. (A) $\times 63$, scale bar 50 μm (B) $\times 20$, scale bar 100 μm .

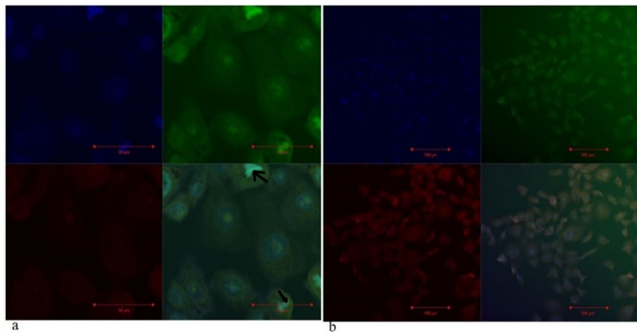


Figure 10: Confocal micrographs of Au-CsCaCO₃NPs treated MCF-7 cells showing cellular uptake and morphology under different fluorescent filters using DAPI (blue), AO (green), PI (red) and merged filter. (A) $\times 63$, scale bar 50 μm (B) $\times 20$, scale bar 100 μm .

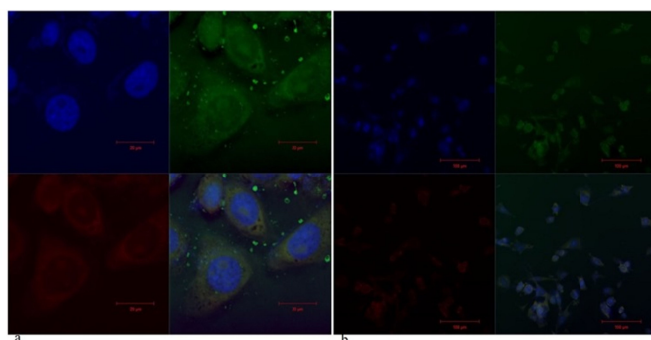


Figure 11: Confocal micrographs of NIH3T3 control showing cellular morphology under different fluorescent filters using DAPI (blue), AO (green), PI (red) and merged filter. (A) $\times 100$, scale bar 20 μm (B) $\times 20$, scale bar 100 μm .

Altogether, these results provide interesting insights into fluorescence and confocal imaging of the Au-

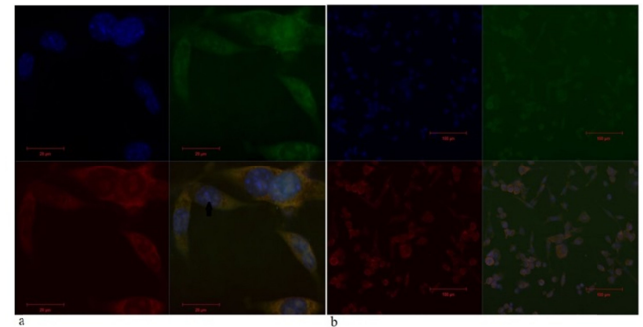


Figure 12: Confocal micrographs of Au-CsCaCO₃NPs treated NIH3T3 cells showing cellular uptake and morphology under different fluorescent filters using DAPI (blue), AO (green), PI (red) and merged filter. (A) $\times 100$, scale bar 20 μm (B) $\times 20$, scale bar 100 μm .

CsCaCO₃NPs treated cells of MCF-7 and NIH3T3 using AO, PI double staining and DAPI. The present study was intended to determine the cell death and cellular uptake of the synthesized nanoparticle where the most obvious finding to arise from the fluorescence imaging is the fact that the MCF-7 treated cells observed more cell deaths in comparison to the NIH3T3 treated cells counterparts as shown in figures 7 and 8. Additionally, from the confocal imaging, it is abundantly clear that the cells were able to take up nanoparticles within their cellular compartments as demonstrated in the figures 9 - 12. These results reflect those of Feng and colleagues (2015) and Yuan and colleagues (2014) who also found that fabricated bio-conjugated nanoparticles confirmed cellular internalization into MCF-7 and MDA-MB-231 over NIH3T3 [101, 102]. Furthermore, these findings are encouragingly in agreement with other studies, in which water soluble fluorescent conjugated polyelectrolytes with self-assembly 3D nanostructures were established to use for bio imaging of cancer and

normal cell lines including MCF-7 and NIH3T3 which also showed comparable figures as well [103]. In addition, the present study also supports similar evidence from Zhang and colleagues (2016) [104] that conjugated nanoparticles were taken up by the treated MCF-7 and NIH3T3 cells. More importantly, the results are in accord with recent studies that confirmed cellular uptake of the nanoparticles, cell death findings and non-toxicity to the normal cell line over the cancer cell line [105-107]. Although these results differ from some published studies [108, 109], they are still consistent with a number of recent works [110-112]. It seems likely that these results could be due to a number of factors affecting the efficiency of the nanoparticles and cellular uptake such as size, shape, charge and surface modification of the nanoparticles, explained by pinocytosis, a type of endocytosis associated with internalization of the nanoparticles. Elaborately, smaller particles such as nanoparticles can easily be internalized by the cell and in regards to shape and charge it has been confirmed that more positive charges and spherical particles are easily taken up by the cell due to the highly negative charge present in the cell membrane [113, 114]. These are useful results and therefore it is safe and possible that our conjugated nanoparticles could be used for bio imaging.

CONCLUSIONS

The goal of this study was to assess biocompatibility and cellular uptake of gold-near infrared conjugated cockle shell-derived calcium carbonate nanoparticles for fluorescent imaging. Based on our results, the

conjugated nanoparticles are biocompatible, environmentally friendly, easily synthesized, and suitable for imaging applications. Additionally, not only were they taken up by both cancer and non-cancerous cell lines, but increased cell death was observed in the cancer cells relative to the non-cancerous cells. Taken together, these findings suggest the possibility of a role for these synthesized conjugated nanoparticles role in cancer imaging. This research extends our knowledge for bio-imaging using gold-cockle shell-derived calcium carbonate nanoparticles.

COMPETING INTERESTS

The authors declare that there are no competing interests regarding the publication of this paper.

FUNDING

This work was financially supported by Fundamental Research Grant Scheme (FRGS) provided by Malaysian Government [Grant Project no. 5524842] and Islamic Development Bank M.Sc. Scholarship Programme, in purchasing all the required reagents and consumables.

AUTHOR CONTRIBUTIONS

All the author(s) contributed equally towards completion of this paper.

ACKNOWLEDGEMENTS

This work was supported by Fundamental Research Grant Scheme (FRGS) provided by Malaysian Government [Grant Project no. 5524842] and Islamic Development Bank M.Sc. Scholarship Programme.

REFERENCES

1. D. Guo, G. Xie, and J. Luo, "Mechanical properties of nanoparticles: Basics and

- applications,” *J. Phys. D. Appl. Phys.*, vol. 47, no. 1, p. 25, 2014.
2. S. Jamal, “Application of Nanoparticles of Ceramics, Peptides, Silicon, Carbon, and Diamonds in Tissue Engineering,” *Chem. Sci. J.*, vol. 4, no. 1, p. 11, 2013.
 3. S. Van Rijt and P. Habibovic, “Enhancing regenerative approaches with nanoparticles,” *J. R. Soc. Interface*, vol. 14, no. 129, p. 20170093, 2017.
 4. R. Wang, J. Lang, Y. Liu, Z. Lin, and X. Yan, “Ultra-small, size-controlled Ni(OH)₂ nanoparticles: elucidating the relationship between particle size and electrochemical performance for advanced energy storage devices,” *NPG Asia Mater.*, vol. 7, no. 6, p. e183, 2015.
 5. F. Y. Kong, J. W. Zhang, R.-F. Li, Z. X. Wang, W. J. Wang, and W. Wang, “Unique Roles of Gold Nanoparticles in Drug Delivery, Targeting and Imaging Applications,” *Molecules*, vol. 22, no. 9, p. 1445, 2017.
 6. Kenry, W. C. Lee, K. P. Loh, and C. T. Lim, “When Stem Cells Meet Graphene: Opportunities and Challenges in Regenerative Medicine,” *Biomaterials*, no. Oct 4, 2017.
 7. N. Volkova, O. Pavlovich, O. Fesenko, O. Budnyk, S. Kovalchuk, and A. Goltsev, “Studies of the Influence of Gold Nanoparticles on Characteristics of Mesenchymal Stem Cells,” *J. Nanomater.*, vol. 2017, p. 9, 2017.
 8. R. T. De Silva, M. M. M. G. P. G. Mantilaka, K. L. Goh, S. P. Ratnayake, G. A. J. Amaratunga, and K. M. N. De Silva, “Magnesium Oxide Nanoparticles Reinforced Electrospun Alginate-Based Nanofibrous Scaffolds with Improved Physical Properties,” *Int. J. Biomater.*, vol. 2017, p. 9, 2017.
 9. G. G. Walmsley et al., “Nanotechnology in bone tissue engineering,” *Nanomedicine*, vol. 11, no. 5, pp. 1253–1263, 2015.
 10. S. Chapman et al., “Nanoparticles for cancer imaging: The good, the bad, and the promise,” *Nano Today*, vol. 8, no. 5, pp. 454–460, 2013.
 11. S. C. Baetke, T. Lammers, and F. Kiessling, “Applications of nanoparticles for diagnosis and therapy of cancer,” *Br. J. Radiol.*, vol. 88, no. 1054, p. 20150207, 2015.
 12. Z. Jaji et al., “Safety assessments of subcutaneous doses of aragonite calcium carbonate nanocrystals in rats,” *J. Nanoparticle Res.*, vol. 19, no. 5, p. 175, 2017.
 13. S. Nicolardi, Y. E. M. Van Der Burgt, J. D. C. Codée, M. Wuhler, C. H. Hokke, and F. Chiodo, “Structural Characterization of Biofunctionalized Gold Nanoparticles by Ultrahigh-Resolution Mass Spectrometry,” *ACS Nano*, vol. 11, no. 8, pp. 8257–8264, 2017.
 14. Shafiu Kamba and Z. A. B. Zakaria, “Osteoblasts growth behaviour on bio-based calcium carbonate aragonite nanocrystal,” *Biomed Res. Int.*, vol. 2014, 2014.
 15. Y. Gao et al., “Effect of Eu³⁺ doping on the structural and photoluminescence properties of cubic CaCO₃,” *Mater. Sci. Eng. B Solid-State Mater. Adv. Technol.*, vol. 203, pp. 52–58, 2016.
 16. M. Yan et al., “Fabrication and photoluminescence properties of TiO₂:Eu³⁺ microspheres with tunable structure from solid to core-shell,” *CrystEngComm*, vol. 16, no. 39, pp. 9216–9223, 2014.
 17. Q. Li, X. Zeng, S. Yang, and X. Liao, “Microwave Synthesis and Photoluminescence Properties of CaMoO₄:Eu³⁺ Nanocomposites,” *Open J. Compos. Mater.*, vol. 7, no. 2, pp. 99–104, 2017.
 18. Biswas, A. T. Nagaraja, and M. J. McShane, “Fabrication of nanocapsule carriers from multilayer-coated vaterite calcium carbonate nanoparticles,” *ACS Appl. Mater. Interfaces*, vol. 6, no. 23, pp. 21193–21201, 2014.
 19. M. S. Savelyeva et al., “Vaterite coatings on

- electrospun polymeric fibers for biomedical applications,” *J. Biomed. Mater. Res. - Part A*, vol. 105, no. 1, pp. 94–103, 2017.
20. T.-H. Nguyen, T. Q. Bao, I. Park, and B.-T. Lee, “A novel fibrous scaffold composed of electrospun porous poly(ϵ -caprolactone) fibers for bone tissue engineering,” *J. Biomater. Appl.*, vol. 28, no. 4, pp. 514–528, 2013.
21. Y. Wen et al., “3D printed porous ceramic scaffolds for bone tissue engineering: a review,” *Biomater. Sci.*, vol. 5, no. 9, pp. 1690–1698, 2017.
22. L. Weng, M. J. Teusink, F. D. Shuler, V. Parecki, and J. Xie, “Highly controlled coating of strontium-doped hydroxyapatite on electrospun poly(ϵ -caprolactone) fibers,” *J. Biomed. Mater. Res. - Part B Appl. Biomater.*, vol. 105, no. 4, pp. 753–763, 2017.
23. S. Mallakpour and E. Khadem, “Chitosan reinforced with modified CaCO₃ nanoparticles to enhance thermal, hydrophobicity properties and removal of Cu(II) and Cd(II) ions,” *J. Polym. Res.*, vol. 24, no. 6, p. 86, 2017.
24. Khalil, N. M. Julkapli, W. A. Yehye, W. J. Basirun, and S. K. Bhargava, Graphene-gold nanoparticles hybrid-synthesis, functionalization, and application in a electrochemical and surface-enhanced raman scattering biosensor, vol. 9, no. 6. 2016.
25. S. Abdolmohammadi et al., “Enhancement of Mechanical and Thermal Properties of Polycaprolactone/Chitosan Blend by Calcium Carbonate Nanoparticles,” *Int. J. Mol. Sci.*, vol. 13, no. 4, pp. 4508–4522, 2012.
26. Muxika, A. Etxabide, J. Uranga, P. Guerrero, and K. de la Caba, “Chitosan as a bioactive polymer: Processing, properties and applications,” *Int. J. Biol. Macromol.*, vol. 105, pp. 1358–1368, 2017.
27. Capek, “Polymer decorated gold nanoparticles in nanomedicine conjugates,” *Adv. Colloid Interface Sci.*, vol. CIS-01716, p. 14, 2017.
28. L. Dziawer et al., “Gold nanoparticle bioconjugates labelled with ²¹¹At for targeted alpha therapy,” *RSC Adv.*, vol. 7, no. 65, pp. 41024–41032, 2017.
29. B. A. Kairdolf, X. Qian, and S. Nie, “Bioconjugated Nanoparticles for Biosensing, in Vivo Imaging, and Medical Diagnostics,” *Anal. Chem.*, vol. 89, no. 2, pp. 1015–1031, 2017.
30. M. K. Uchiyama et al., “In vivo and In vitro toxicity and anti-inflammatory properties of gold nanoparticle bioconjugates to the vascular system,” *Toxicol. Sci.*, vol. 142, no. 2, pp. 497–507, 2014.
31. R. Singh, S. Patil, N. Singh, and S. Gupta, “Dual functionality nanobioconjugates targeting intracellular bacteria in cancer cells with enhanced antimicrobial activity,” *Sci. Rep.*, vol. 7, no. 1, p. 5792, 2017.
32. Kapur et al., “Self-Assembled Gold Nanoparticle-Fluorescent Protein Conjugates as Platforms for Sensing Thiolate Compounds via Modulation of Energy Transfer Quenching,” *Bioconjug. Chem.*, vol. 28, no. 2, pp. 678–687, 2017.
33. A. Hondred et al., “Enhanced enzymatic activity from phosphotriesterase trimer gold nanoparticle bioconjugates for pesticide detection,” *Analyst*, vol. 142, pp. 3261–3271, 2017.
34. R. Xing et al., “Colloidal Gold-Collagen Protein Core-Shell Nanoconjugate: One-Step Biomimetic Synthesis, Layer-by-Layer Assembled Film, and Controlled Cell Growth,” *ACS Appl. Mater. Interfaces*, vol. 7, no. 44, pp. 24733–24740, 2015.
35. R. Del Caño et al., “Hemoglobin bioconjugates with surface-protected gold nanoparticles in aqueous media: The stability depends on solution pH and protein properties,” *J. Colloid Interface Sci.*, vol. 505, pp. 1165–1171, 2017.
36. X. Huang, P. K. Jain, I. H. El-Sayed, and M.

- A. El-Sayed, "Plasmonic photothermal therapy (PPTT) using gold nanoparticles," *Lasers Med. Sci.*, vol. 23, no. 3, pp. 217–228, 2008.
37. E. Boisselier and D. Astruc, "Gold nanoparticles in nanomedicine: preparations, imaging, diagnostics, therapies and toxicity," *Chem. Soc. Rev.*, vol. 38, no. 6, pp. 1759–1782, 2009.
38. E. C. Dreaden, L. A. Austin, M. A. Mackey, and M. A. El-Sayed, "Size matters: gold nanoparticles in targeted cancer drug delivery," *Ther. Deliv.*, vol. 3, no. 4, pp. 457–478, 2012.
39. P. John Thomas, "Nanoparticles," *Annu. Reports Sect. "A" (Inorganic Chem.*, vol. 108, p. 493, 2012.
40. Y.-C. Yeh, B. Creran, and V. M. Rotello, "Gold nanoparticles: preparation, properties, and applications in bionanotechnology," *Nanoscale*, vol. 4, no. 6, pp. 1871–80, 2012.
41. G. M. F. Calixto, J. Bernegossi, L. M. de Freitas, C. R. Fontana, and M. Chorilli, "Nanotechnology-Based Drug Delivery Systems for Photodynamic Therapy of Cancer: A Review," *Molecules*, vol. 21, no. 3, p. 342, 2016.
42. Wei et al., "Yolk/Shell Assembly of Gold Nanoparticles by Size Segregation in Solution," *J. Am. Chem. Soc.*, vol. 138, no. 10, pp. 3274–3277, 2016.
43. P. Lisha and T. Pradeep, "Enhanced visual detection of pesticides using gold nanoparticles," *J. Environ. Sci. Health. B.*, vol. 44, no. 7, pp. 697–705, 2009.
44. B. Stephen Inbaraj and B. H. Chen, "Nanomaterial-based sensors for detection of foodborne bacterial pathogens and toxins as well as pork adulteration in meat products," *J. Food Drug Anal.*, vol. 24, no. 1, pp. 15–28, 2016.
45. Y. Gao et al., "Amphiphilic PEGylated Lanthanide-Doped Upconversion Nanoparticles for Significantly Passive Accumulation in the Peritoneal Metastatic Carcinomatosis Models Following Intraperitoneal Administration," *ACS Biomater. Sci. Eng.*, vol. 3, no. 9, pp. 2176–2184, 2017.
46. S. D. Li and L. Huang, "Pharmacokinetics and biodistribution of nanoparticles," *Mol. Pharm.*, vol. 5, no. 4, pp. 496–504, 2008.
47. R. a Petros and J. M. DeSimone, "Strategies in the design of nanoparticles for therapeutic applications," *Nat. Rev. Drug Discov.*, vol. 9, no. 8, pp. 615–627, 2010.
48. L. Markman, A. Rekechenetskiy, E. Holler, and J. Y. Ljubimova, "Nanomedicine therapeutic approaches to overcome cancer drug resistance," *Adv. Drug Deliv. Rev.*, vol. 65, no. 13–14, pp. 1866–1879, 2013.
49. R. K. Jain, "Transport of Molecules, Particles, and Cells in Solid Tumors," *Annu. Rev. Biomed. Eng.*, vol. 1, no. 1, pp. 241–263, 1999.
50. J. F. Verhoef and T. J. Anchordoquy, "Questioning the use of PEGylation for drug delivery," *Drug Deliv. Transl. Res.*, vol. 3, no. 6, pp. 499–503, 2013.
51. H. Peng et al., "Preparation of hierarchical mesoporous CaCO₃ by a facile binary solvent approach as anticancer drug carrier for etoposide," *Nanoscale Res. Lett.*, vol. 8, no. 1, p. 321, 2013.
52. T. Lammers, W. E. Hennink, and G. Storm, "Tumour-targeted nanomedicines: principles and practice," *Br. J. Cancer*, vol. 99, no. 3, pp. 392–397, 2008.
53. H.-C. Huang, S. Barua, G. Sharma, S. K. Dey, and K. Rege, "Inorganic nanoparticles for cancer imaging and therapy," *J. Control. Release*, vol. 155, no. 3, pp. 344–357, 2011.
54. H. Maeda, J. Wu, T. Sawa, Y. Matsumura, and K. Hori, "Tumor vascular permeability and the EPR effect in macromolecular therapeutics: A review," *J. Control. Release*,

- vol. 65, no. 1–2, pp. 271–284, 2000.
55. J. Turkevich, P. . Stevenson, and J. Hiller, “Synthesis of Gold Nanoparticles Turkevich method,” *Discuss. Faraday Soc.*, vol. 11, pp. 55–75, 1951.
 56. N. Islam et al., “A novel catalytic method for the synthesis of spherical aragonite nanoparticles from cockle shells,” *Powder Technol.*, vol. 246, pp. 434–440, 2013.
 57. H. N. Verma, P. Singh, and R. M. Chavan, “Gold nanoparticle: Synthesis and characterization,” *Vet. World*, vol. 7, no. 2, pp. 72–77, 2014.
 58. W.-Y. Cai, Q. Xu, X.-N. Zhao, J.-J. Zhu, and H.-Y. Chen, “Porous Gold-Nanoparticle–CaCO₃ Hybrid Material: Preparation, Characterization, and Application for Horseradish Peroxidase Assembly and Direct Electrochemistry,” *Chem. Mater.*, vol. 18, no. 2, pp. 279–284, 2006.
 59. Allen, P. Millett, E. Dawes, and N. Rushton, “Lactate dehydrogenase activity as a rapid and sensitive test for the quantification of cell numbers in vitro,” *Clin. Mater.*, vol. 16, no. 4, pp. 189–194, 1994.
 60. S. M. Smith, M. B. Wunder, D. A. Norris, and Y. G. Shellman, “A simple protocol for using a LDH-Based cytotoxicity assay to assess the effects of death and growth inhibition at the same time,” *PLoS One*, vol. 6, no. 11, p. e26908, 2011.
 61. K. Cho, H. Chang, D. S. Kil, B. G. Kim, and H. D. Jang, “Synthesis of dispersed CaCO₃ nanoparticles by the ultrafine grinding,” *J. Ind. Eng. Chem.*, vol. 15, no. 2, pp. 243–246, 2009.
 62. Eaqub Ali, M. Ullah, and S. Bee Abd Hamid, “Surfactant-Assisted Ball Milling: a Novel Route To Novel Materials With Controlled Nanostructure -a Review,” *Rev. Adv. Mater. Sci.*, vol. 37, pp. 1–14, 2014.
 63. H. Schmidt, “Nanoparticles by chemical synthesis, processing to materials and innovative applications,” *Appl. Organomet. Chem.*, vol. 15, no. 5, pp. 331–343, 2001.
 64. H. Jazayeri, H. Amani, A. A. Pourfatollah, H. Pazoki-Toroudi, and B. Sedighimoghaddam, “Various methods of gold nanoparticles (GNPs) conjugation to antibodies,” *Sens. Bio-Sensing Res.*, vol. 9, pp. 17–22, 2016.
 65. Rawat, Y. S. Rajput, M. K. Bharti, and R. Sharma, “A method for synthesis of gold nanoparticles using 1-amino-2-naphthol-4-sulphonic acid as reducing agent,” *Curr. Sci.*, vol. 110, no. 12, pp. 2–5, 2016.
 66. Raoof et al., “Stability of antibody-conjugated gold nanoparticles in the endo- lysosomal nanoenvironment: Implications for non-invasive radiofrequency-based cancer therapy,” *Nanomedicine*, vol. 8, no. 7, pp. 1096–1105, 2013.
 67. K. Lata, A. K. Jaiswal, L. Naik, and R. Sharma, “Gold Nanoparticles : Preparation , Characterization and Its Stability in Buffer,” *J. Nanotechnol. its Appl.*, vol. 17, no. 1, pp. 1–10, 2015.
 68. E. Hoque, M. Shehryar, and K. N. Islam, “Material Science & Engineering Processing and Characterization of Cockle Shell Calcium Carbonate (CaCO₃) Bioceramic for Potential Application in Bone Tissue Engineering,” *J. Mater. Sci. Engeneering*, vol. 2, no. 4, pp. 2–6, 2013.
 69. Tabrizi, F. Ayhan, and H. Ayhan, “Gold nanoparticle synthesis and characterisation,” *Hacettepe J. Biol. Chem.*, vol. 37, no. 3, pp. 217–226, 2009.
 70. Maji et al., “Spectroscopic interaction study of human serum albumin and human hemoglobin with Mersilea quadrifolia leaves extract mediated silver nanoparticles having antibacterial and anticancer activity,” *J. Mol. Struct.*, vol. 1141, pp. 584–592, 2017.
 71. U. Stolarczyk, K. Stolarczyk, Ł. Marta, M. Kubiszewski, A. Le, and O. Michalak, “Pemetrexed conjugated with gold

- nanoparticles – Synthesis , characterization and a study of noncovalent interactions,” *Eur. J. Pharm. Sci.*, vol. 109, no. June, pp. 13–20, 2017.
72. R. K. Salar and N. Kumar, “Synthesis and characterization of vincristine loaded folic acid–chitosan conjugated nanoparticles,” *Resour. Technol.* 2, vol. 2, no. 4, pp. 199–214, 2016.
 73. H. Zhang et al., “Fabrication of genistein-loaded biodegradable TPGS-b-PCL nanoparticles for improved therapeutic effects in cervical cancer cells,” *Int. J. Nanomedicine*, vol. 10, pp. 2461–2473, 2015.
 74. Y. Zhang et al., “Zeta potential: A surface electrical characteristic to probe the interaction of nanoparticles with normal and cancer human breast epithelial cells,” *Biomed. Microdevices*, vol. 10, no. 2, pp. 321–328, 2008.
 75. S. Das, W. K. Ng, P. Kanaujia, S. Kim, and R. B. H. Tan, “Formulation design, preparation and physicochemical characterizations of solid lipid nanoparticles containing a hydrophobic drug: Effects of process variables,” *Colloids Surfaces B Biointerfaces*, vol. 88, no. 1, pp. 483–489, 2011.
 76. T. Isa et al., “Antibacterial activity of ciprofloxacin-encapsulated cockle shells calcium carbonate (Aragonite) nanoparticles and its biocompatibility in macrophage J774A.1,” *Int. J. Mol. Sci.*, vol. 17, p. 713, 2016.
 77. W. B. Tan and Y. Zhang, “Study of chitosan coatings on nanoparticles for biomedical applications,” *Int. J. Nanosci.*, vol. 3, no. 04n05, pp. 685–689, 2004.
 78. M. Smith, M. C. Mancini, and S. Nie, “Second window for in vivo imaging,” *Nat. Nanotechnol.*, vol. 4, no. 11, pp. 710–711, 2009.
 79. G. Bao, S. Mitragotri, and S. Tong, “Multifunctional nanoparticles for drug delivery and molecular imaging,” *Annu. Rev. Biomed. Eng.*, vol. 15, no. April, pp. 253–82, 2013.
 80. S. F. Khattak, M. Spataro, L. Roberts, and S. C. Roberts, “Application of colorimetric assays to assess viability, growth and metabolism of hydrogel-encapsulated cells,” *Biotechnol. Lett.*, vol. 28, no. 17, pp. 1361–1370, 2006.
 81. Legrand et al., “Lactate dehydrogenase (LDH) activity of the number of dead cells in the medium of cultured eukaryotic cells as marker,” *J. Biotechnol.*, vol. 25, no. 3, pp. 231–243, 1992.
 82. S. M. Chowdhury, S. Xie, J. Fang, S. K. Lee, and B. Sitharaman, “Nanoparticle-Facilitated Membrane Depolarization-Induced Receptor Activation: Implications on Cellular Uptake and Drug Delivery,” *ACS Biomater. Sci. Eng.*, vol. 2, no. 12, pp. 2153–2161, 2016.
 83. E. Elshawy, E. A. Helmy, and L. A. Rashed, “Preparation, Characterization and in Vitro Evaluation of the Antitumor Activity of the Biologically Synthesized Silver Nanoparticles,” vol. 5, no. 5, pp. 149–166, 2016.
 84. S. Gurunathan, J. W. Han, V. Eppakayala, M. Jeyaraj, and J. H. Kim, “Cytotoxicity of biologically synthesized silver nanoparticles in MDA-MB-231 human breast cancer cells,” *Biomed Res. Int.*, vol. 2013, p. 10, 2013.
 85. Lanari et al., “Five Novel Hormone-responsive Cell Lines Derived from Murine Mammary Ductal Carcinomas : In Vivo and in Vitro Effects of Estrogens and Progestins,” *Cancer Res.*, vol. 1, pp. 293–302, 2001.
 86. A.-S. H. Abdullah, A. S. Mohammed, R. Abdullah, M. E. S. Mirghani, and M. Al-Qubaisi, “Cytotoxic effects of *Mangifera indica* L. kernel extract on human breast cancer (MCF-7 and MDA-MB-231 cell lines) and bioactive constituents in the cr

- ude extract.," *BMC Complement. Altern. Med.*, vol. 14, no. 1, p. 199, 2014.
87. J. Koren et al., "Rhodacyanine derivative selectively targets cancer cells and overcomes tamoxifen resistance," *PLoS One*, vol. 7, no. 4, 2012.
88. S. Mullick Chowdhury, G. Lalwani, K. Zhang, J. Y. Yang, K. Neville, and B. Sitharaman, "Cell specific cytotoxicity and uptake of graphene nanoribbons," *Biomaterials*, vol. 34, no. 1, pp. 283–293, 2013.
89. Y. Zhang et al., "Cytotoxicity Effects of Graphene and Single-Wall Carbon Nanotubes in Neural Phaeochromocytoma-Derived PC12 Cells," *Am. Chemcial Soc.*, vol. 4, no. 6, pp. 3181–3186, 2010.
90. Seabra and N. Durán, "Nanotoxicology of Metal Oxide Nanoparticles," *Metals (Basel)*, vol. 5, no. 2, pp. 934–975, 2015.
91. M. Gruhlke, C. Nicco, F. Batteux, and A. Slusarenko, "The Effects of Allicin, a Reactive Sulfur Species from Garlic, on a Selection of Mammalian Cell Lines," *Antioxidants*, vol. 6, no. 1, p. 1, 2016.
92. M.-Y. Liou and P. Storz, "Reactive oxygen species in cancer," *Antioxidants*, vol. 4, no. 5, 2010.
93. L. B. Sullivan and N. S. Chandel, "Mitochondrial reactive oxygen species and cancer," *Cancer Metab.*, vol. 2, no. 1, p. 17, 2014.
94. T. P. Szatrowski and C. F. Nathan, "Production of Large Amounts of Hydrogen Peroxide by Human Tumor Cells," *Cancer Res.*, vol. 51, no. 3, pp. 794–798, 1991.
95. E.-J. Park, J. Yi, K.-H. Chung, D.-Y. Ryu, J. Choi, and K. Park, "Oxidative stress and apoptosis induced by titanium dioxide nanoparticles in cultured BEAS-2B cells," *Toxicol. Lett.*, vol. 180, no. 3, pp. 222–229, 2008.
96. L. Minai, D. Yeheskely-Hayon, and D. Yelin, "High levels of reactive oxygen species in gold nanoparticle-targeted cancer cells following femtosecond pulse irradiation," *Sci. Rep.*, vol. 3, no. 1, p. 2146, 2013.
97. P. Fu, Q. Xia, H.-M. Hwang, P. C. Ray, and H. Yu, "Mechanisms of nanotoxicity: Generation of reactive oxygen species," *J. Food Drug Anal.*, vol. 22, no. 1, pp. 64–75, 2014.
98. G. Saravanakumar, J. Kim, and W. J. Kim, "Reactive-Oxygen-Species-Responsive Drug Delivery Systems: Promises and Challenges," *Adv. Sci.*, vol. 4, no. 1, p. 1600124, 2017.
99. Y. Xue, T. Zhang, B. Zhang, F. Gong, Y. Huang, and M. Tang, "Cytotoxicity and apoptosis induced by silver nanoparticles in human liver HepG2 cells in different dispersion media," *J. Appl. Toxicol.*, vol. 36, no. 3, pp. 352–360, 2016.
100. W. Zhang et al., "Prussian Blue Nanoparticles as Multienzyme Mimetics and Reactive Oxygen Species Scavengers," *J. Am. Chem. Soc.*, vol. 138, no. 18, pp. 5860–5865, 2016.
101. G. Feng, J. Liu, J. Geng, and B. Liu, "Conjugated polymer microparticles for selective cancer cell image-guided photothermal therapy," *J. Mater. Chem. B*, vol. 3, no. 6, pp. 1135–1141, 2015.
102. Y. Yuan, G. Feng, W. Qin, B. Z. Tang, and B. Liu, "Targeted and image-guided photodynamic cancer therapy based on organic nanoparticles with aggregation-induced emission characteristics," *Chem Commun*, vol. 50, no. 63, pp. 8757–8760, 2014.
103. K. Y. Pu and B. Liu, "Fluorescent conjugated polyelectrolytes for bioimaging," *Adv. Funct. Mater.*, vol. 21, no. 18, pp. 3408–3423, 2011.
104. Y.-H. Zhang, Y.-M. Zhang, Y. Yang, L.-X. Chen, and Y. Liu, "Controlled DNA condensation and targeted cellular imaging by ligand exchange in a polysaccharide–quantum dot conjugate," *Chem. Commun.*, vol. 52, no. 36, pp. 6087–6090, 2016.
105. K. Li and B. Liu, "Polymer-encapsulated

- organic nanoparticles for fluorescence and photoacoustic imaging,” *Chem. Soc. Rev.*, vol. 43, no. 18, pp. 6570–97, 2014.
106. J. Geng, K. Li, K. Y. Pu, D. Ding, and B. Liu, “Conjugated polymer and gold nanoparticle Co-loaded PLGA nanocomposites with eccentric internal nanostructure for dual-modal targeted cellular imaging,” *Small*, vol. 8, no. 15, pp. 2421–2429, 2012.
107. K. Li et al., “Folic acid-functionalized two-photon absorbing nanoparticles for targeted MCF-7 cancer cell imaging,” *Chem. Commun. (Camb.)*, vol. 47, no. 26, pp. 7323–7325, 2011.
108. L. A. Muehlmann, B. C. Ma, J. P. F. Longo, M. F. de M. Almeida Santos, and R. B. Azevedo, “Aluminum-phthalocyanine chloride associated to poly(methyl vinyl ether-co-maleic anhydride) nanoparticles as a new third-generation photosensitizer for anticancer photodynamic therapy,” *Int. J. Nanomedicine*, vol. 9, no. 1, pp. 1199–1213, 2014.
109. J. Li, J. You, Y. Dai, M. Shi, C. Han, and K. Xu, “Gadolinium oxide nanoparticles and aptamer-functionalized silver nanoclusters-based multimodal molecular imaging nanoprobe for optical/magnetic resonance cancer cell imaging,” *Anal. Chem.*, vol. 86, no. 22, pp. 11306–11311, 2014.
110. Z. Li et al., “Ultrasmall water-soluble and biocompatible magnetic iron oxide nanoparticles as positive and negative dual contrast agents,” *Adv. Funct. Mater.*, vol. 22, no. 11, pp. 2387–2393, 2012.
111. K. Li et al., “Conjugated polymer based nanoparticles as dual-modal probes for targeted in vivo fluorescence and magnetic resonance imaging,” *Adv. Funct. Mater.*, vol. 22, no. 15, pp. 3107–3115, 2012.
112. B. Yang, X. Zhang, X. Zhang, Z. Huang, Y. Wei, and L. Tao, “Fabrication of aggregation-induced emission based fluorescent nanoparticles and their biological imaging application: Recent progress and perspectives,” *Mater. Today*, vol. 19, no. 5, pp. 284–291, 2016.
113. S. Salatin and A. Yari Khosroushahi, “Overviews on the cellular uptake mechanism of polysaccharide colloidal nanoparticles,” *J. Cell. Mol. Med.*, vol. XX, no. X, pp. 1–19, 2017.
114. K. T. Thurn et al., “Nanoparticles for applications in cellular imaging,” *Nanoscale Res. Lett.*, vol. 2, no. 9, pp. 430–441, 2007.